

RESEARCH

Open Access



Brain alterations and neurologic disorder progression induced by lymphatic dysfunction in the head and neck region

Hwayeong Cheon¹, Dong-Cheol Woo^{2,3}, Seungwoo Cha⁴, Yeon Ji Chae³, Inhee Maeng⁵, Seung Jae Oh^{5*} and Jae Yong Jeon^{1,4*}

Abstract

The potential negative impact of lymphatic dysfunction caused by head and neck cancer treatment remains underexplored. Emerging evidence suggests that waste clearance and fluidic balance in the brain are connected to the peripheral lymphatic system in the head and neck region, implying that lymphatic injury in this area could contribute to brain damage. This study aimed to investigate the pathological alterations in the brain induced by peripheral lymphatic dysfunction in the head and neck region using the lymphatic obstruction animal model. An animal model underwent cervical lymph node dissection combined with radiation therapy to simulate the condition with the peripheral lymphatic dysfunction in the head and neck region after cancer treatment. Lymphatic drainage impairment in the head and neck region was associated with significant swelling, disrupted lymphatic drainage, and immune cell infiltration in the white matter. The imaging techniques revealed ventricular enlargement and increased brain water content caused by fluid imbalance leading to significant structural alterations in the brain. Histopathological analysis demonstrated structural brain alterations similar to that of hydrocephalus and cerebral edema, while rotarod tests showed a substantial decline in motor performance. These findings highlight the impact of peripheral lymphatic dysfunction on brain integrity and function. This study provides evidence that brain damage in head and neck cancer patients may be influenced not only by chemotherapy or radiotherapy but also by lymphatic dysfunction caused by surgical interventions. Lymphatic injury in the head and neck region emerges as a potential risk factor for brain damage, underscoring the need for further research into preventive and therapeutic strategies.

Keywords Head & neck cancer, Lymphatic dysfunction, Neurological disorder, Cerebrospinal fluid accumulation, Immune cell infiltration, Hydrocephalus, Brain edema

*Correspondence:

Seung Jae Oh
issac@yuhs.ac
Jae Yong Jeon
jyjeon71@gmail.com

¹Rehabilitation Research Center, Biomedical Engineering Research Center, Asan Institute for Life Sciences, Asan Medical Center, Seoul, Republic of Korea

²Department of Convergence Medicine, Asan Medical Center, University of Ulsan College of Medicine, Seoul, Republic of Korea

³Convergence Medicine Research Center, Asan Institute for Life Sciences, Asan Medical Center, Seoul, Republic of Korea

⁴Department of Rehabilitation Medicine, Asan Medical Center, University of Ulsan College of Medicine, 88, Olympic-ro 43-gil, Songpa-gu, Seoul 05505, Republic of Korea

⁵College of Medicine, YUHS-KRIBB Medical Convergence Research Institute, Yonsei University, Seoul 03722, Republic of Korea



© The Author(s) 2025. **Open Access** This article is licensed under a Creative Commons Attribution-NonCommercial-NoDerivatives 4.0 International License, which permits any non-commercial use, sharing, distribution and reproduction in any medium or format, as long as you give appropriate credit to the original author(s) and the source, provide a link to the Creative Commons licence, and indicate if you modified the licensed material. You do not have permission under this licence to share adapted material derived from this article or parts of it. The images or other third party material in this article are included in the article's Creative Commons licence, unless indicated otherwise in a credit line to the material. If material is not included in the article's Creative Commons licence and your intended use is not permitted by statutory regulation or exceeds the permitted use, you will need to obtain permission directly from the copyright holder. To view a copy of this licence, visit <http://creativecommons.org/licenses/by-nc-nd/4.0/>.

Introduction

Head and neck cancers (HNC) have an annual global incidence of around 930,000 cases, accounting for approximately 5% of all cancer cases in 2020 [1]. These cancers are not only prevalent but also highly lethal with a significant number of patients experiencing severe complications post-treatment. Among these complications, cognitive and behavioral impairments are particularly concerning, affecting memory, attention, and behavior due to brain damage. This neurotoxicity severely reduces survivors' quality of life. The risk factors for brain damage in HNC patients are considered to be largely attributed to chemotherapy and radiotherapy in cancer treatments. Chemotherapy particularly agents like cisplatin and radiation therapy targeting the head and neck region can damage healthy brain tissues, and lead to neuroinflammation, oxidative stress, and disruption of brain white matter integrity [2, 3]. However, because the surgical site is distant from the brain, the possibility of brain damage caused by surgical procedures such as lymph node dissection has not been widely considered, although these surgeries are among the most commonly performed in HNC treatment. Recent research has revealed that fluid circulation in the brain is connected to the peripheral cervical lymphatic system [4]. This raises the possibility that lymphatic drainage impairments in the head and neck region resulting from lymph node dissection could also pose a risk factor for brain damage. This discovery opens up new avenues for understanding potential complications in the brain associated with lymphatic surgeries. The lymphatic system serves both as the circulatory and immune systems. The collapse of the lymphatic system leads to fluidic imbalance, infiltration of immune cells, and inflammation in the affected area. In the case of the head and neck, cervical lymph nodes (CLNs) are important peripheral junctions for lymphatic circulation, encompassing regions including the brain [5]. CLNs are the major drainage routes for cerebrospinal fluid (CSF) flowing through the nasal cavity into the lymphatic system, highlighting the importance of CLNs in fluid circulation and immune function [4, 6–9]. They play an important role in the head and neck by filtering and transporting the fluid from the CSF. Therefore, CLN dissection (CLND) for HNC treatment can lead to lymphatic dysfunction in that region, thereby increasing CSF levels and infiltrating immune cells in the central nervous system (CNS). The recent discovery of lymphatic circulation in the CNS has sparked interest in its role in fluid balance, waste clearance, immune response regulation, and neurological disease pathogenesis [10–13]. Several studies on CNS lymphatics have focused on the onset of neurodegenerative diseases, which are associated with the excretion of neurotoxic materials [14–17]. However, peripheral lymphatic dysfunction in the head and neck

region also may involve an inflammation mechanism that can lead to other neurological disorders. Lymphatic circulation disorders and the resulting disruption of fluidic balance are major causes of lymphedema, and the occurrence of lymphedema leads to immune cell infiltration and inflammation at the affected site [18, 19]. Therefore, lymphatic obstruction in the head and neck region potentially leads to impaired CSF drainage creating a condition similar to lymphedema within the brain, which could trigger the development of neurological diseases. In clinical settings, lymphedema occurs when the dominant lymph nodes in each lymphatic territory are damaged or removed because of lymphatic injury, such as lymph node dissection. Therefore, we hypothesized that CSF accumulation caused solely by CLND may lead to pathophysiological and histopathological alterations in the brain, potentially triggering neurological disorders.

To validate our hypothesis, we produced animal models with lymphatic dysfunction in the head and neck region via superficial and deep CLN (SCLN and DCLN) dissection and radiation to investigate pathophysiological alterations in the brain. Therefore, complete removal of the SCLN and DCLN is likely to induce head and neck (or cervical) lymphedema. We then used preclinical magnetic resonance imaging (MRI) and terahertz (THz) spectroscopic imaging systems to measure the increased CSF and water content in the brain in the animal models. We investigated the pathological changes in brain tissue in response to changes in brain water content and evaluated motor coordination and fatigue resistance through the rotarod behavior test.

Materials and methods

All experiments were conducted in accordance with the relevant guidelines and regulations of the Institutional Animal Care and Use Committee (IACUC) of our institution (2022-12-110 and 2023-30-226). The IACUC abides by the Institute of Laboratory Animal Resources and Animal Research: Reporting of in vivo Experiments guidelines of the National Center for the Replacement, Refinement, and Reduction of Animals in Research.

Production of animal models of lymphatic obstruction in the head and neck region

All animals were given free access to water and food and were kept under stable humidity and temperature. This study included 27 male Sprague–Dawley rats weighing 280–320 g (8–9 weeks old). 15 animals were divided into two groups: 12 in the CLND group and 3 in the control group for imaging and histological examination. The remaining 12 animals were divided into two diagnostic criterion for specific disease groups of 6 each for the CLND and the control group to perform the rotarod test. The rats were fed adaptively for 1 week before surgery,

and all procedures involving animal experiments were conducted in specific designated areas. The development of animal models of lymphedema for preclinical research is still an actively researched area, but the fundamental surgical and radiation protocols followed the methods used for producing extremity lymphedema animal models [20–23] based on the research by Daneshgaran et al. [24]. Before surgery, animals were anesthetized with a mixture of tiletamine/zolazepam (Zoletil 50) (50 mg/kg; Virbac, France) and xylazine (Rompun, Bayer Korea, Seoul, Republic of Korea) at a volume ratio of 5:1 after induction with 4% isoflurane gas. During anesthesia, electric clippers were used to remove fur from the cheek and neck.

The same investigator operated on all animals. After disinfecting the surgical area with 75% ethyl alcohol, microsurgical procedures for lymph node dissection were performed. A circumferential skin incision was made on the ventral side of the neck. Subsequently, 0.05 mL Evans blue (Sigma Aldrich Co., MO, USA) solution (30 mg/mL in 0.9% saline) was subcutaneously injected into the lower lip and both ears, enabling CLN visualization. SCLNs are circularly arranged around the submandibular glands of the masseter muscle and are connected by collecting lymphatic vessels that extend from the cervical region [25]. SCLNs (lymph nodes 1–3, Additional file 1: Figure S1A) are sequentially connected to DCLNs along the lymphatic vessels that collect the fluid (lymph node 4, Additional file 1: Figure S1A). After visualization using Evans blue solution, the lymph nodes were carefully removed from the deep surface with subcutaneous fat to minimize iatrogenic damage. Given that the nerve plexus, major veins, and arteries are distributed around the CLNs, we exercised caution during incision and cauterization to avoid damaging the adjacent tissues (Additional file 1: Figure S1B).

After the procedure, the skin edges were sutured using the folding suture method, bringing the skin surfaces into contact with each other to prevent intradermal lymphatic vessel reconnection. The skin incision was circumferentially cauterized before suturing. Ketoprofen (1 mg/kg; SCD Ketoprofen Inj., SamChunDang Pharm, Seoul, Republic of Korea) was administered intramuscularly immediately after the surgery. On postoperative day 2, the surgical site, including the neck area, was irradiated with a single dose of 20 Gy using an X-Rad 320 device (Precision X-Ray Inc., CT, Madison, WI, USA). The remaining parts of the body, including the head, were shielded with customized 8-mm thick lead plates (99% radiation shielding) to protect them from radiation exposure. Animals were anesthetized with 4% isoflurane gas before irradiation and placed in the prone position. A cumulative radiation dose of 20 Gy was delivered in 10 fractions at a rate of 1 Gy/min. Only animals with

successful model formation, which was determined by evaluating edema onsets and lymphatic drainage, were used for the experiment 1 week after radiation exposure, while the rest were sacrificed. We precisely induced peripheral lymphatic dysfunction in the head and neck region using microsurgical techniques and radiation while minimizing damage to other tissues. Therefore, the experimental group (CLND group) consisted of animal models representing edema/swelling and abnormal lymphatic drainage due to CLND and radiation exposure, whereas the control group comprised animals in normal conditions.

Cervical edema evaluation and lymphatic drainage in NIRF-ICGL

In previous studies, the development of lymphedema in animal models was verified via limb circumference or thickness measurement [26, 27]. In this study, changes in the cervical cross-sectional area were used to evaluate edema. We estimated the cervical cross-sectional area based on the anatomy of the rats, assuming an elliptical shape with the vertebra in the middle. Lateral and ventral images of the neck were consistently measured and analyzed from the same posture, and the cross-sectional area was calculated according based on the neck diameter using ImageJ software (ImageJ 1.48 v, <http://rsbweb.nih.gov/ij/>; NIH, Bethesda, MD, USA). After anesthesia, the animals were flexed on a plane in a completely relaxed state, and the diameter of the neck was measured using a customized near-infrared imager (Additional file 1: Figure S2) [21, 28–30].

Near-infrared fluorescence indocyanine green lymphangiography (NIRF-ICGL) is the primary technique for evaluating lymphatic drainage, allowing real-time imaging of lymphatic function and flow. We employed NIRF-ICGL to determine the condition of cervical lymphatic drainage [31]. As hair scattered infrared light, the animals were sedated using 4% isoflurane gas, and the hair on the region of interest was removed using electric clippers and depilatory cream to facilitate an accurate observation of fluorescence images. Subsequently, 3 μ L of indocyanine green (ICG) powder (Diagnogreen Injection 25 mg; Daiichi Sankyo co., LTD, Tokyo, Japan) mixed with 25 mg/ml bovine serum albumin solution (20 μ g/ml; Sigma, St. Louis, MO) was intradermally injected into the lower lip using 34-gauge needles. In clinical practice, abnormal lymph drainage patterns are detected using NIRF-ICGL in patients with lymphedema. An ICG contrast agent injected into the lymphatic system can be detected because it emits fluorescence light when excited by an external near-infrared light source. Based on the clinical standards for dermal backflow staging, abnormal lymphatic drainage patterns are categorized as splash, stardust/diffuse, or blackout. In normal lymphatic

circulation, most of the fluid collects and flows through collective lymphatic vessels in a linear pattern. The splash pattern represents dermal backflow in the superficial pathway. Stardust/diffuse patterns caused by lymphatic accumulation and leakage indicate severe lymphedema. Finally, the blackout pattern indicates the absence of lymphatic drainage due to obstruction.

Dermal backflow staging shows that severe lymphedema also resulted in an increased lymphatic leakage into the surrounding tissues, thereby causing the linear ICG fluorescence image to become planar (Additional file 1: Figure S3). Given that such changes increase the bright area (an area where contrast agents spread) in the images, the severity of lymphedema can be measured by calculating the area. In this experiment, we quantified the bright areas in the images obtained from NIRF-ICGL based on the measurement of areas with intensity values greater than the median in the grayscale histogram using the automatic threshold function in ImageJ software (Additional file 1: Figure S4). The images were acquired at a constant height of 25 cm from a fixed position. In addition, we measured lymphatic contraction signals in the same collective lymphatic vessels in both groups. In a previous study, we examined a method for obtaining lymphatic contraction signals through signal processing and identified variations in lymphatic contraction signals caused by lymphatic obstruction [28]. Lymphatic obstruction in the animals used in this study was evaluated using these variations in lymphatic contraction. Therefore, we obtained 15-minute real-time videos to identify these variations in lymphatic contraction and extracted lymphatic contraction signals in both groups using ImageJ software. fast Fourier transform (FFT) signal processing was performed using Origin Pro 9 software (Origin 9.0; OriginLab, Northampton, MA, USA) for numerical calculations and visualization based on previous research [28].

Volumetric analysis of the brain using MRI

In the animal models, an increase in CSF levels in the brain with lymphedema was verified 2 and 8 weeks after surgery and radiation using high-precision MRI. In the CNS, the CSF flows through a system of fluid-filled cavities known as the ventricular system. CSF drainage disturbance increases CSF pressure within the ventricular system, leading to an abnormal increase in its volume [32, 33]. To measure the volume of the ventricular system, MRI was performed using a 7.0 T Bruker preclinical MRI scanner (PharmaScan 70/16; Bruker BioSpin GmbH, Germany) with a 72-mm transmit volume coil and a rat brain surface receiver coil. All the animals were anesthetized with 1.5–2.5% isoflurane in a mixture of 70% nitrous oxide and 30% oxygen administered through a nose cone. A warm-water circulating flatbed was used

to maintain their body temperature at 37.5 ± 0.5 °C, and they were consistently monitored for stable breathing. T2-weighted images (T2-WIs) were acquired using a fast spin-echo sequence (TR, 5250 ms; TE, 66 ms; averages, 1; echo spacing, 11 ms; field of view, 25 × 25 mm; slice thickness, 1.0 mm; slice number, 27). MRI images were analyzed using ImageJ software. lateral ventricle (LV) volume was calculated as the sum of LV areas measured across multiple MRI slices. Herein, the total brain and LV volumes were measured using T2-WIs and the two-dimensional volumetric technique, which involves adding the volume measured from each slice.

THz spectroscopic imaging to measure water content in the brain sections

CLND-induced lymphatic obstruction was identified based on edema/swelling and abnormal lymphatic drainage in the head and neck region. Next, we observed changes in the hydration of freshly excised brain tissues using THz reflectance in THz spectroscopic imaging. A previous study has demonstrated that water content in the brain tissue measured by THz spectroscopy agreed with traditional tissue water mass measurement methods [34]. Therefore, THz spectroscopic imaging has the potential not only to quantify brain tissue water content but also to visualize its distribution within the tissue. Considering that important pathophysiological changes often lead to increased tissue water content which may serve as a diagnostic criterion for specific diseases [35–37], THz spectroscopic imaging could offer information on brain alteration induced by lymphatic obstruction.

The THz spectroscopic imaging system used to measure the brain tissue water content consisted of an ultrashort pulsed laser with a center wavelength of 1560 nm and two fiber-coupled antenna modules (FC/APC) for the emitter/detector. For the laser radiation, the repetition rate was 100 MHz, and the pulse width was 60 fs. The laser generated approximately 60 mW of power at the output of the polarization-maintaining fiber. The laser beam was divided by a beam-splitter fiber and guided to the emitter and detector. The emitter antenna (Tx; TERA 15-TX-FC; Menlo Systems GmbH, Planegg, Germany) had a line pattern on a Fe: InGaAs/InAlAs substrate and was equipped with a PM PANDA fiber patch cord (I=100 cm, FC/APC connector). THz waves were generated from the emitter with an 80-V direct current bias. The THz waves were incident vertically on two polymethylpentene (TPX) lenses (L1 and L2) on the sample holder by a metal mirror (M1), reflected off the sample, and guided into the detector by a Si beam splitter (THz BS) and TPX lens (L3) (Additional file 1: Figure S5). The detector antenna (Rx; TERA 15-RX-FC; Menlo Systems GmbH, Planegg, Germany) had a dipole pattern on an LT InGaAs/InAlAs substrate with the same fiber

patch cord as the emitter. THz pulses were acquired by the pump-probe sampling method using a fast scan delay with a resonance frequency of 20 Hz and a scan range of 30 ps. The THz pulses were recorded automatically by a computer using a low-noise current preamplifier and data acquisition board. THz spectroscopic images of the sample with a spatial resolution of $250 \times 250 \mu\text{m}$ per pixel were obtained using two-dimensional raster scanning. We extracted THz spectroscopic images at this frequency using the FFT of the time-domain signals. The samples were placed on a quartz window with a diameter of 30 mm and a thickness of 3 mm.

Eight weeks after surgery and radiation, brain samples including the cerebrum and cerebellum were harvested, and the weight of the brain without the meninges was measured. The brain tissues, including the cortex, white matter tract, hippocampus, and thalamus, were subsequently sectioned. The location of the sections was determined by referencing section levels 2 and 3 from the study by Rao et al. or section levels 3 and 4 from the study by Garman et al. [38, 39]. The section levels were labeled based on the findings of Garman et al. After slicing in the coronal direction of the brain at section levels 3 and 4, based on the study by Garman et al. [38, 39], THz spectroscopic images were measured as quickly as possible. The sample holder containing the brain sections was sealed during scanning to prevent the tissues from drying. The samples were placed on a 2-inch quartz window for measurements using the THz spectroscopic imaging system in reflection mode. The window containing the brain tissue was sealed in a small box to prevent the sample from drying out. The sample holder was connected to two high-resolution mechanical stages, allowing for two-dimensional movement (horizontal x-y plane). This enabled images to be obtained using raster scanning with 250- μm spatial resolution. The THz spectroscopic images were analyzed separately for peak-to-peak and individual frequency-based images.

Histological analysis

At 8 weeks postoperatively, the animals were euthanized using carbon dioxide asphyxiation, and whole brain tissues were harvested and preserved in 10% buffered formalin for 24 h at 4 °C. This was followed by a minimum of 48 h of decalcification using Calci-Clear Rapid (National Diagnostics, Atlanta, GA, USA) histological decalcifying reagent. Brain sections were also taken at the same location as the THz spectroscopic imaging sections. The samples were embedded in paraffin blocks and then sectioned into 3- μm -thick slices before staining with hematoxylin and eosin (H&E). The tissue sections were examined using a 20 objective microscope equipped with an integrated camera (Olympus B53, Tokyo, Japan). Tissue density was determined by scanning and digitally

processing H&E-stained slide images. All brain sections were acquired for comparison with THz spectroscopic images. All images were processed and assessed using Olympus Cellsens Standard ver. 1.13 software (Olympus, Tokyo, Japan). The following antibodies were used for immunohistochemical staining of brain sections: rabbit monoclonal CD11c C-terminal (1:200; ab52632, Abcam, Cambridge, UK) as a dendritic cell (DC) marker and rabbit monoclonal CD4 (1:200; ab133616, Abcam, Cambridge, UK), which is a T-cell receptor marker. All slides were imaged using a light microscope (Model BX40, Olympus, Tokyo, Japan). During imaging, the cell nucleus area was measured and quantified by selecting three regions from brain sections prepared from three rats in each group using the color threshold function of ImageJ software.

Accelerating rotarod test

The rotarod system for rats (Ugo Basile S.R.L., Gemonio, Italy) was used to evaluate the performance of motor function and coordination. After a one-week resting period following model formation, training was conducted for two days followed by testing at both 2 and the 8 weeks. During the training phase, the animals were placed on the rotarod rotating at 3 rpm for 5 min, followed by a 5-minute rest. This cycle was repeated twice, after which they were trained on the rotarod rotating at 10 rpm for 5 min, concluding the training session. If an animal fell off the rod, it was returned to its cage. During the testing phase, the animals were habituated in the behavior lab room for 1 h after being transferred from the animal room. Following the habituation, the training sequence was repeated, and the behavior test was conducted after a 5-minute rest. The rotarod speed was gradually accelerated from 3 rpm to 60 rpm over 999 s in the test. When the animal fell, a sensor in the basket detected the fall and automatically recorded the time and speed at which the fall occurred. A total of 6 trials were measured with a 5-minute rest interval.

Statistical analysis

All the statistical analyses were performed using GraphPad Prism 9 (GraphPad Software Inc., Boston, MA, USA) and Microsoft Excel 2019 version 2111 (Microsoft Corporation, Redmond, WA, USA). Student's t-tests were used to compare differences between groups. A p-value of less than 0.05 was considered to indicate a statistically significant disparity.

Results

Volume evaluation in the cervical area

Edema or swelling is the most common diagnostic criterion for lymphedema. In the animal models used in this study, edema was observed in the cervical area and cheeks 1 week after CLND and radiation, and

consistently maintained during the follow-up period (Additional file 1: Figure S6). To quantify the degree of edema, we compared the CLND group with the control group. The CLND group showed an approximately 30% increase in neck cross-sectional area compared with that in the control group ($p < 0.05$) (Fig. 1). This indicated that significant cervical lymphedema occurred in the CLND animal model.

Evaluation of CLN obstruction and increased CSF levels

Subsequently, we verified whether the edema observed in the animal models resulted from lymphatic obstruction due to CLND. In the control group animals, lymphatic flow occurred in the most rostrally located SCLNs along the collective lymphatic vessels in the head and neck region before draining into subsequent CLNs. However, in the CLND group animals, abnormal lymphatic drainage patterns (splash and stardust) were observed throughout the ventral area, including the neck and face. Lymphatic fluid gradually flowed along the net-shaped (splash-patterned) collateral superficial lymphatic vessels. However, dermal backflow due to obstructed lymphatic drainage was observed (Fig. 2a). The CLND group had a significantly higher degree of lymphatic drainage than the control group (Fig. 2b) (* $p < 0.05$).

Furthermore, abnormal waveforms of lymphatic contraction were observed in the CLND group. A previous study showed a change in lymphatic contraction induced by lymphatic obstruction in upper limb models [28]. Figure 2c demonstrates a disruption of the lymphatic circulation in the head and neck region. In the CLND group,

we observed a waveform change and an increase in the frequency of lymphatic contractions compared with those in the control group. The control group presented a more robust lymphatic contraction frequency than the CLND group, which was verified by transforming the time-domain data in Fig. 2c into a frequency-domain spectrum through FFT signal processing. The control group showed regular lymphatic contractions with a peak frequency between 0.1 and 0.2 Hz (Fig. 2d). In contrast, the CLND group showed irregular contractions owing to the disturbances caused by these robust movements.

Volume measurements and NIRF-ICGL demonstrated lymphatic obstruction in the head and neck region of the CLND group. Since CSF drainage is known to be closely related to lymphatic drainage through the CLN, we investigated whether this lymphatic obstruction in the head and neck region increases CSF levels. In the animal models, MRI was used to compare the LV volume change in the CLND and control groups. Figure 2e presents representative images from slice numbers 13 and 17 among multiple MRI slices used to measure brain and LV volume. The LV volume in the CLND group increased by approximately 15% compared with that in the control group at 2 weeks and 8 weeks postoperatively (Fig. 2f). Furthermore, in the CLND group, the LV to whole brain volume ratio increased from 3.8 to 4.7% and 4.4%. MRI results indicated an increase in CSF volume in the CLND group, suggesting a corresponding increase in brain tissue hydration.

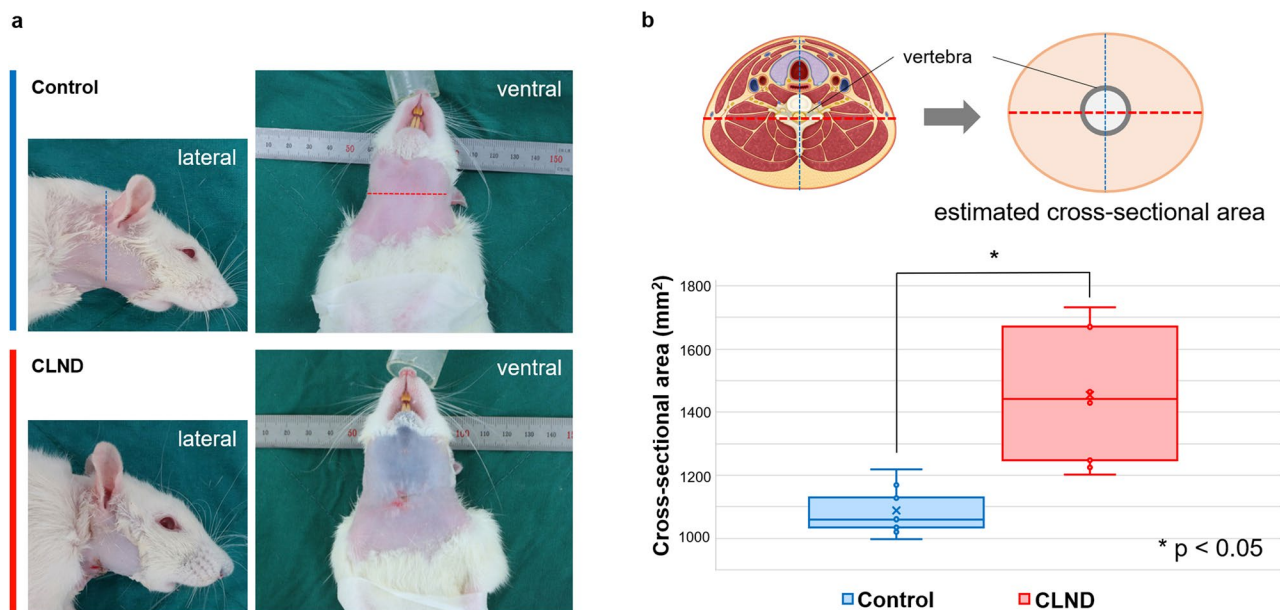


Fig. 1 Measurement of neck circumference changes following CLND. (a) Lateral and ventral views in the cervical region for the control and CLND groups. (b) Neck cross-sectional area for the control and CLND groups. The shape of the neck cross-section is assumed to be an ellipse centered on the vertebra, based on cervical anatomy. The cross-sectional area differs significantly between both groups (t-test, * $p < 0.05$)

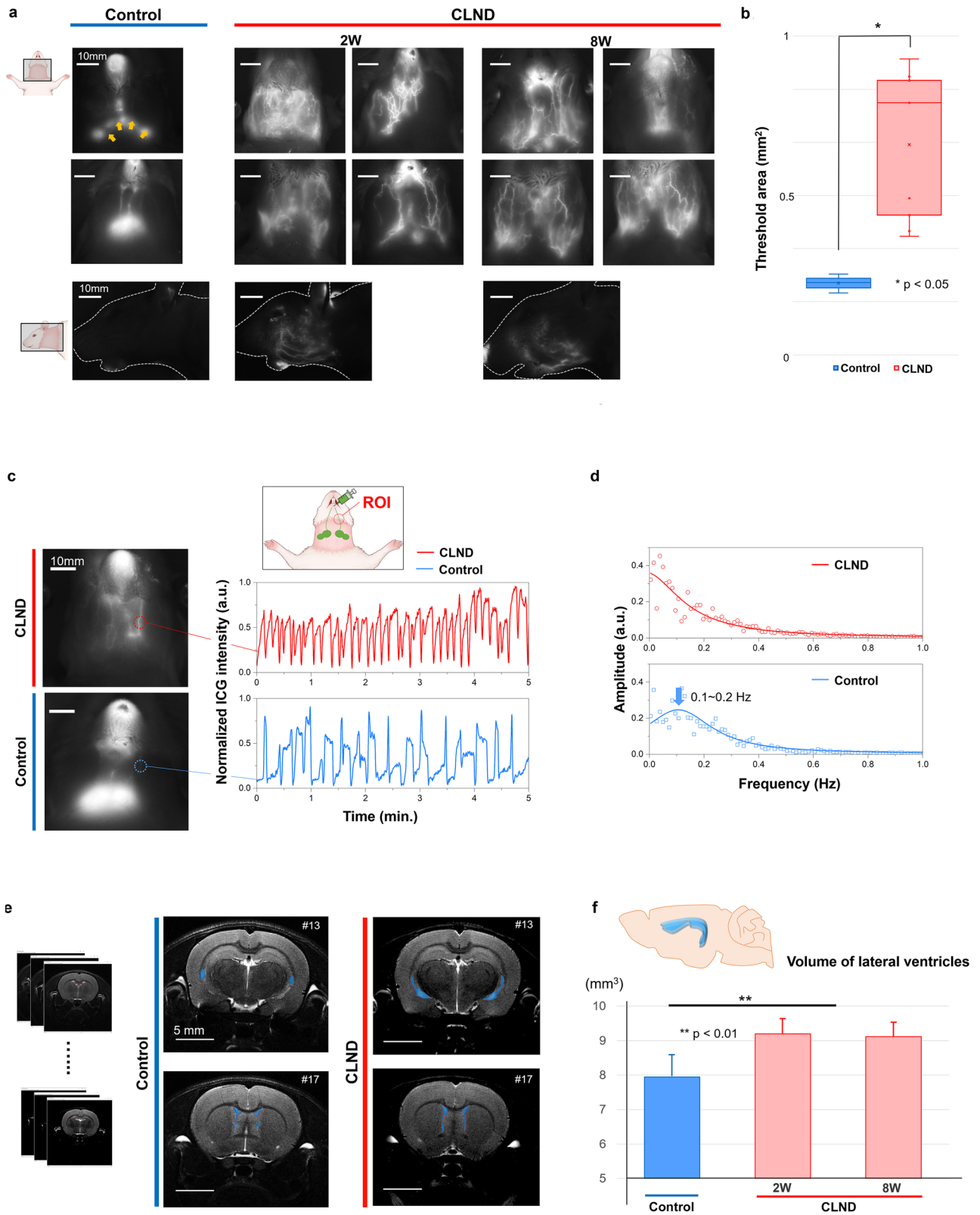


Fig. 2 (See legend on next page.)

(See figure on previous page.)

Fig. 2 Measurement of lymphatic obstruction using NIRF-ICGL and CSF level increase using MRI. **(a)** Lymphatic drainage in the cervical region of control and CLND group animals (at 2 and 8 weeks) using NIRF-ICGL. In the control group, the lymphatic flows along the collective lymphatic vessels toward the CLNs (yellow arrows). In the CLND group, the CLNs are not found, and abnormal lymphatic drainage patterns are observed in the neck and face at 2 and 8 weeks after surgery owing to lymphatic obstruction. **(b)** Quantitative results of lymphatic drainage spread. The threshold area is significantly different between the groups (t-test, $*p < 0.05$). **(c)** The time-domain waveforms of lymphatic contractions measured in the regions of interest (ROI, red dotted circle) of each group. Compared with the control group, the waveform and frequency of lymphatic contractions are alternated in the CLND group. **(d)** Signal conversion from the time-domain to the frequency-domain spectrum via fast Fourier transform (FFT) signal processing. In the control group, signal peaks are observed between 0.1 and 0.2 Hz, indicating frequent movements with a consistent period. **(e)** The images of # 13 and 17 slides among 27 MRI sections are used to measure the volume of the lateral ventricle in the control and CLND groups. The area within the red line represents the lateral ventricle. **(f)** The volume of the lateral ventricle (LV) determined by MRI in the control and CLND groups at 2 weeks and 8 weeks after model formation. The volume of the LV in the CLND group increased by approximately 15% compared with that of the control group (at 2 and 8 weeks), indicating an increase in CSF levels (t-test, $**p < 0.01$)

Evaluation of brain water content

Before preparing brain tissue slides for THz spectroscopic imaging, the entire brain was weighed after harvesting from the animal (Fig. 3a). The brain weight in the CLND group animals was approximately 11% higher than that in the control group; however, the difference was not statistically significant. Figure 3b shows reflectance images of the brain tissue sections of level 3 and 4 obtained using THz peak-to-peak values. The sectional location was based on references to previous research [38, 39]. The CLND group animals showed a higher proportion of red and white areas, indicative of a higher water content within the tissue, than the control group animals. The individual frequency imaging at 0.5, 1.0, and 1.5 THz showed that the 0.5 THz reflectance of brain tissue in the CLND group was significantly higher than that in the control group (Additional file 1: Figure S7). This result indicates an increase in brain tissue water content in the CLND group animals. This is attributed to the sensitivity of the lower-frequency bands in the THz range, which can detect more changes in water content caused by the higher refractive index of water molecules [40–42]. Based on the results of the individual frequency images, the difference between the two groups in the THz spectroscopic images was derived from the difference in THz reflectance caused by the brain tissue water content. The spectral images were reconstructed into binary THz spectroscopic images based on higher (red) and lower (blue) water contents (Fig. 3c). Although high water content was only detected around the LV of brain tissue in the control group, we observed an increase in water content throughout a wider area in the CLND group. These changes were more distinct in the level 4 section than in the level 3 section. In the binary images, the red areas indicate regions with an average increase in water content of approximately 5–6% compared with the blue areas based on individual frequency imaging and the integral values of the spectrum at each pixel point (Fig. 3d).

Histological alterations in brain tissue

The red area in Fig. 4a represents the region where the water content was relatively high in THz spectroscopy,

which was overlaid with the brain tissue section for pathological examination. The locations of the LV and third ventricle (TV), where the CSF accumulates, are closely associated with the distribution of tissues with increased water content. In the control group animals, the tissues surrounding the LV and TV were more hydrated which was similar to the results obtained with brain section images. However, the CLND group animals showed an increase in water content over the wider brain area, including the ventricular region.

Based on these images, we investigated brain tissue changes, focusing on areas with significant changes in water content on THz spectroscopy: the meninges, cerebral cortex (CC), and white matter (WM) (Fig. 4b). In the meninges, where many meningeal lymphatics are present, the CLND group exhibited more partial meningeal edema than the control group. This was more visible at 8 weeks after surgery and radiation than at 2 weeks. The overall tissue density decreased, and many pyknotic nuclei and cellular edema were observed in the CC. The corpus callosum of the WM also showed changes in tissue and density. These histological changes were more prominent at 8 weeks than at 2 weeks in both the CC and WM (Fig. 4c). Figure 4c shows the quantitative results of the cell nucleus area in the CC and WM in the control and CLND groups (2 and 8 weeks). A decrease in the number of cells was observed in both the CC and WM regions in the CLND group animals compared with the control group animals. In addition, the CLND group showed a more significant difference in the number of brain tissue cells in the CC and WM at 8 weeks than at 2 weeks ($*** p < 0.005$, $** p < 0.01$, and n.s. = not significant).

Given the changes in periventricular water content and ventricular expansion, we also investigated the presence of any characteristic periventricular histopathological alterations. All structures associated with ventricles showed an overall decrease in tissue density of the periventricular white matter (PVWM) and a reduction of ventral internal capsule (VIC) structure. Specifically, the ependymal cells lining at the internal surface of the ventricular space were enlarged parallel in the ventricle area. Similar to the histological changes in Fig. 5, these

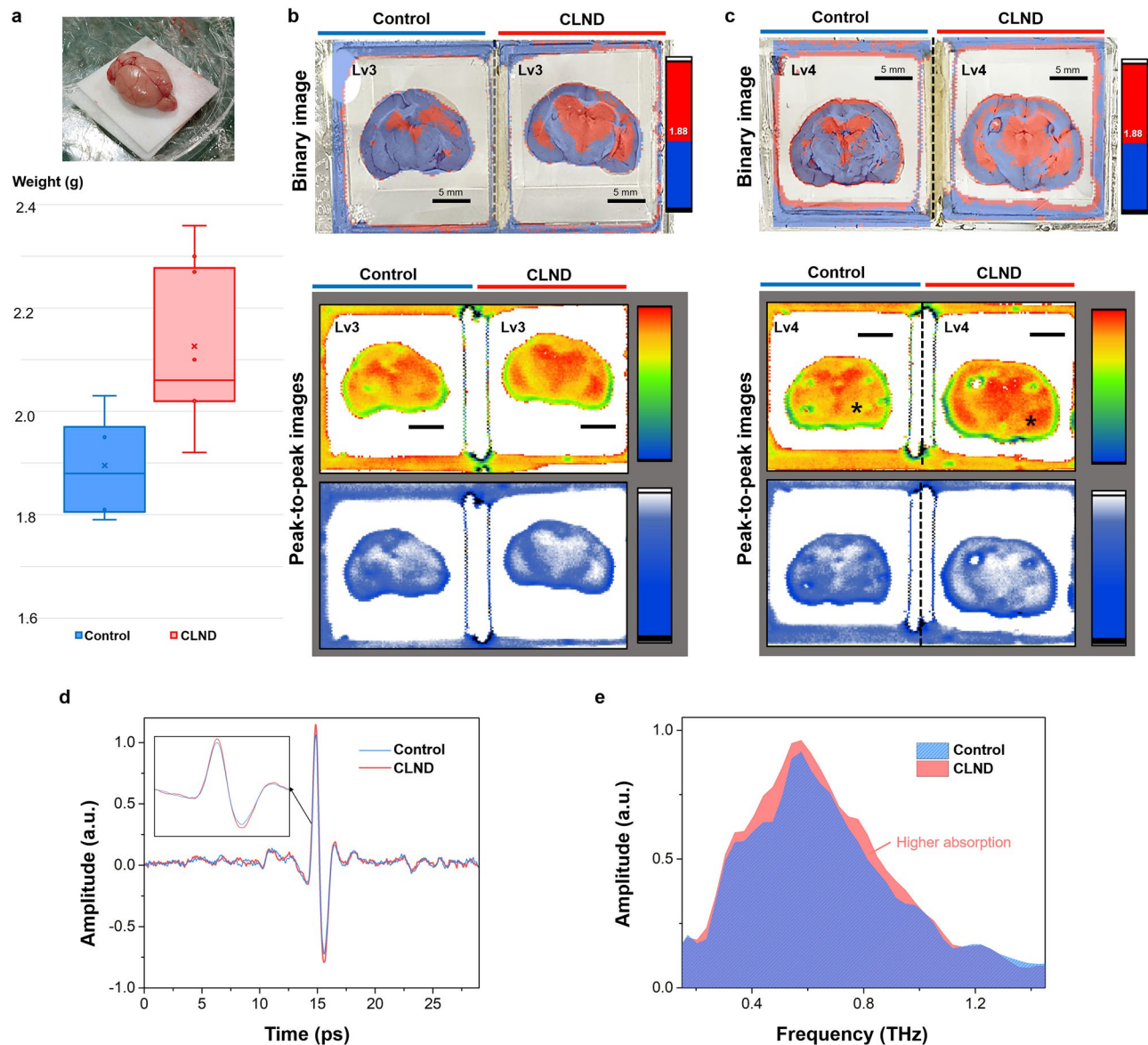


Fig. 3 THz imaging of brain changes following cervical lymph node dissection (CLND). **(a)** The brain section locations of levels 3 and 4 and the weight of the whole brain are measured immediately after extraction from the animals in each group. **(b)** The peak-to-peak THz reflectance images of the brain sections are represented by the rainbow and blue-white gradual values. **(c)** The overlay visible light imaging combined with THz reconstructed binary imaging (higher level: red, lower level: blue) of sectional brain sections. The CLND group at 8 weeks shows a widely higher reflectance than the control group in both sectional levels. **(d)** Time- and **(e)** frequency-domain THz spectra of the pixels marked with black asterisks in control and CLND group images of Fig. 3C. The area outside the overlapping region indicates greater absorption. All scale bars of THz images **(b)** and **(c)** are 5 mm

changes were more prominently observed at 8 weeks than at 2 weeks.

Immune cell infiltration in brain tissue

We investigated the infiltration of immune cells in the same sectional areas shown in Figs. 5 and 6 using antibodies against CD11 and CD4. As shown in Fig. 6a and Figure S8, only a few immune cells were detected in the brain tissue of control group animals. It was difficult to detect DCs in most WM regions, including the PVWM, inferior colliculus, and cerebral peduncle (Additional file

1: Figure S8). However, numerous immune cells were observed to infiltrate the brain tissues in the CLND group animals, and the number of the infiltrated immune cells in the brain increased progressively from 2 weeks to 8 weeks (Additional file 1: Figure S9). Specifically, the infiltration of DCs, a type of immune cell marked by CD11c, increased primarily around the WM region (Fig. 6b).

Latency of fall in the rotarod test

The rotarod test was conducted to evaluate whether these histopathological alterations in the CLND group affected

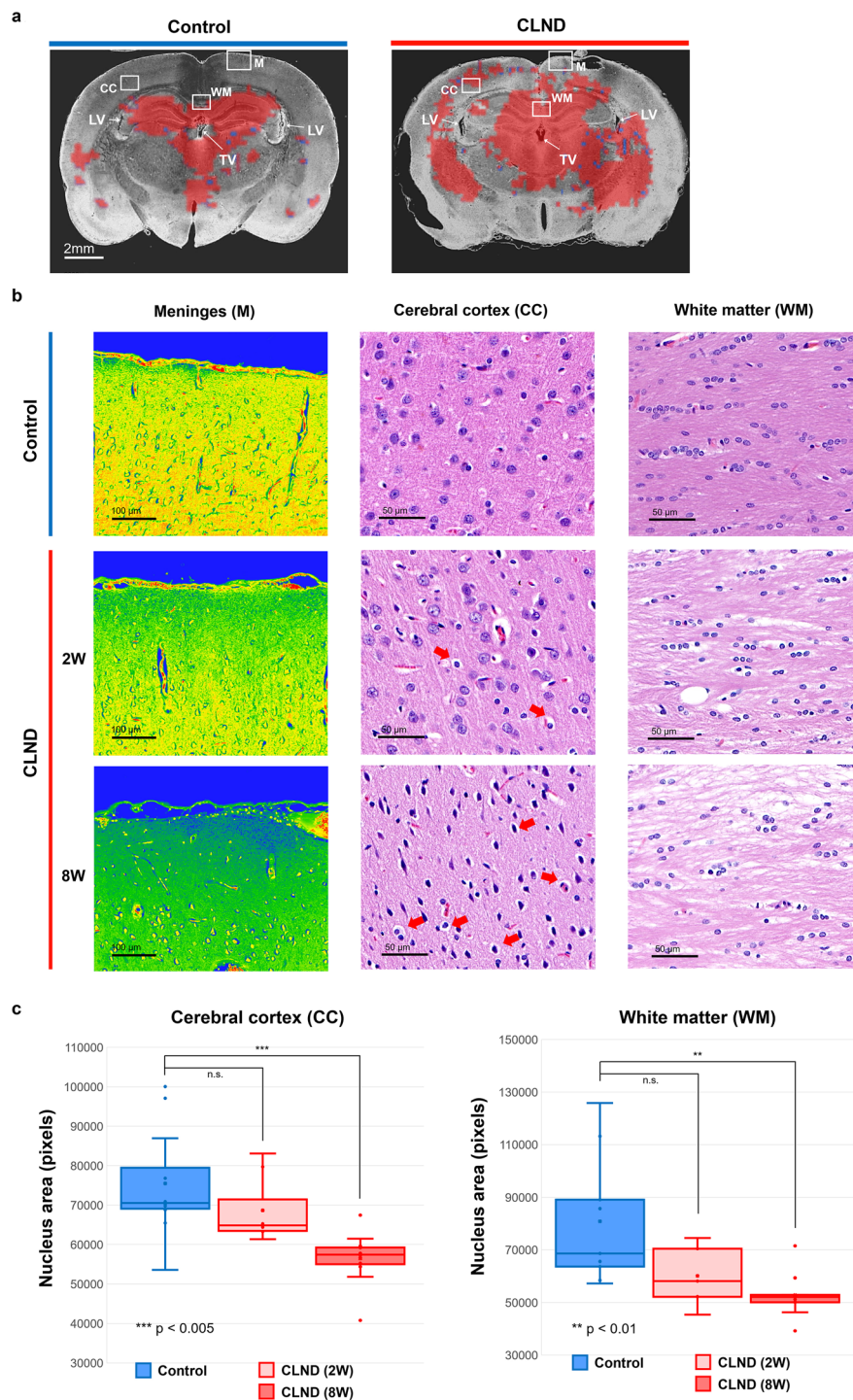


Fig. 4 Histological brain tissue alterations in the cervical lymph node dissection (CLND) group. **(a)** The merged images between the region of high-water content by measuring THz imaging and fixed tissue in the paraffin block. The structural alterations in brain tissue are primarily investigated around regions with differences in water content: meninges (M), cerebral cortex (CC), and white matter (WM) of the corpus callosum. LV: lateral ventricle, TV: third ventricle. **(b)** Tissue structure comparisons in each section. In the CLND group, a decrease in peripheral brain tissue density is observed along with meningeal edema. In the cerebral cortex of CLND animals, many apoptotic cells are identified, including considerable tissue density reduction (red arrows). A decrease in the tissue capsule is observed in the WM of CLND animals. These changes are more noticeable at 8 weeks (8W) than at 2 weeks (2W). **(c)** Quantification of the cell nucleus areas in the CC and WM regions of animals in each group. At 8W, the CLND group shows a significant difference in cell nucleus area compared with the control group (t-test, ** $p < 0.01$ and *** $p < 0.001$)

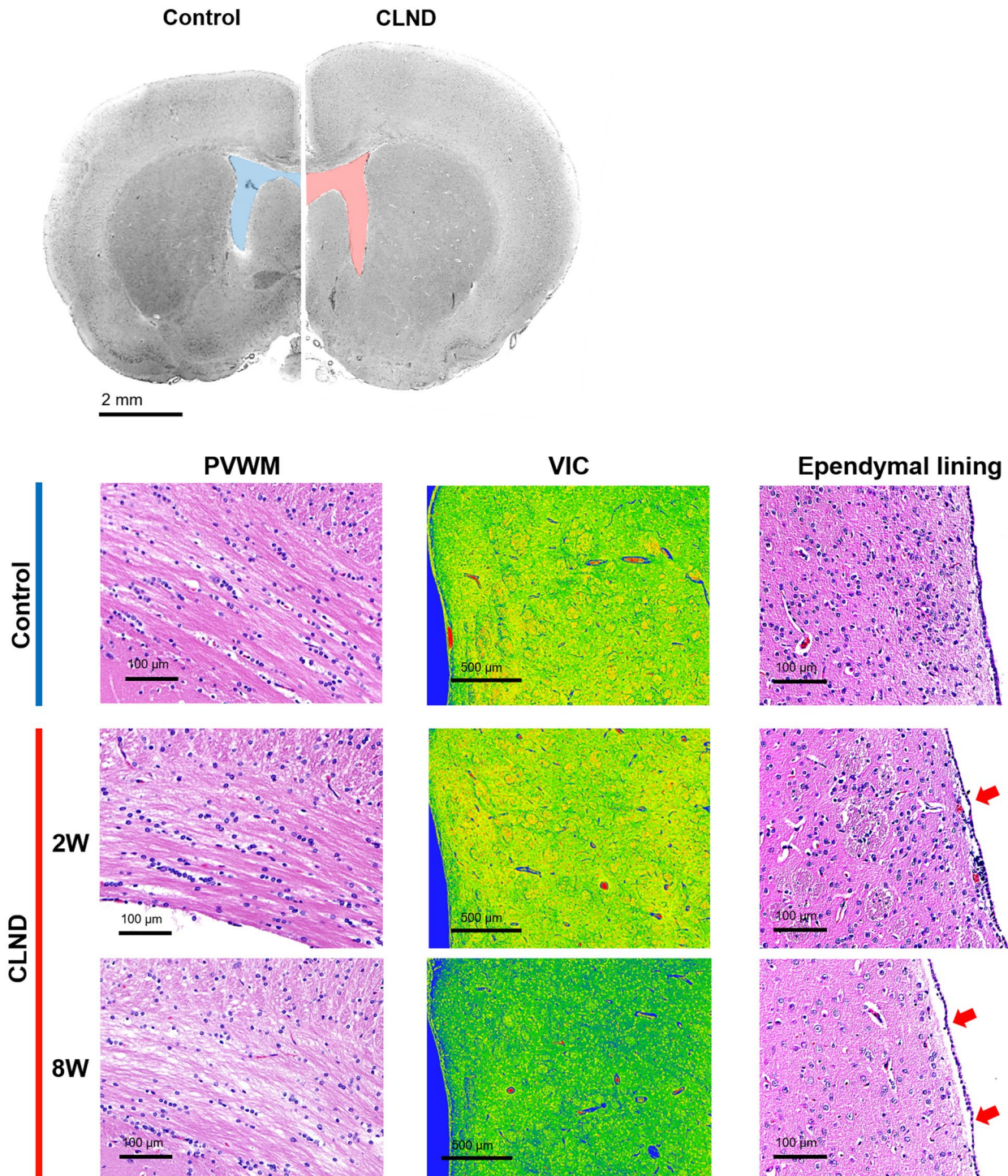


Fig. 5 Increase in ventricular volume and associated periventricular tissue alterations in CLND animals. In the periventricular white matter (PVWM), there is an overall decrease in density as the tissue spacing widens, and a decrease in the structure of the ventral internal capsule (VIC) is identified. Additionally, an enlargement of the ependymal cell lining is observed. These changes are more pronounced at 8 weeks (8W)

the animals' behavior comparing the performance of the normal control group. At 2 weeks and 8 weeks, the CLND group showed a shorter fall latency than the control group. The difference between the groups was particularly significant at 8 weeks compared to 2 weeks (**

$p < 0.01$, *** $p < 0.005$, and **** $p < 0.001$) (Fig. 7a). Overall, the CLND group showed a significant difference in rotarod performance compared to the control group at both 2 weeks and 8 weeks (**** $p < 0.001$). The control group showed average values in latency of fall of

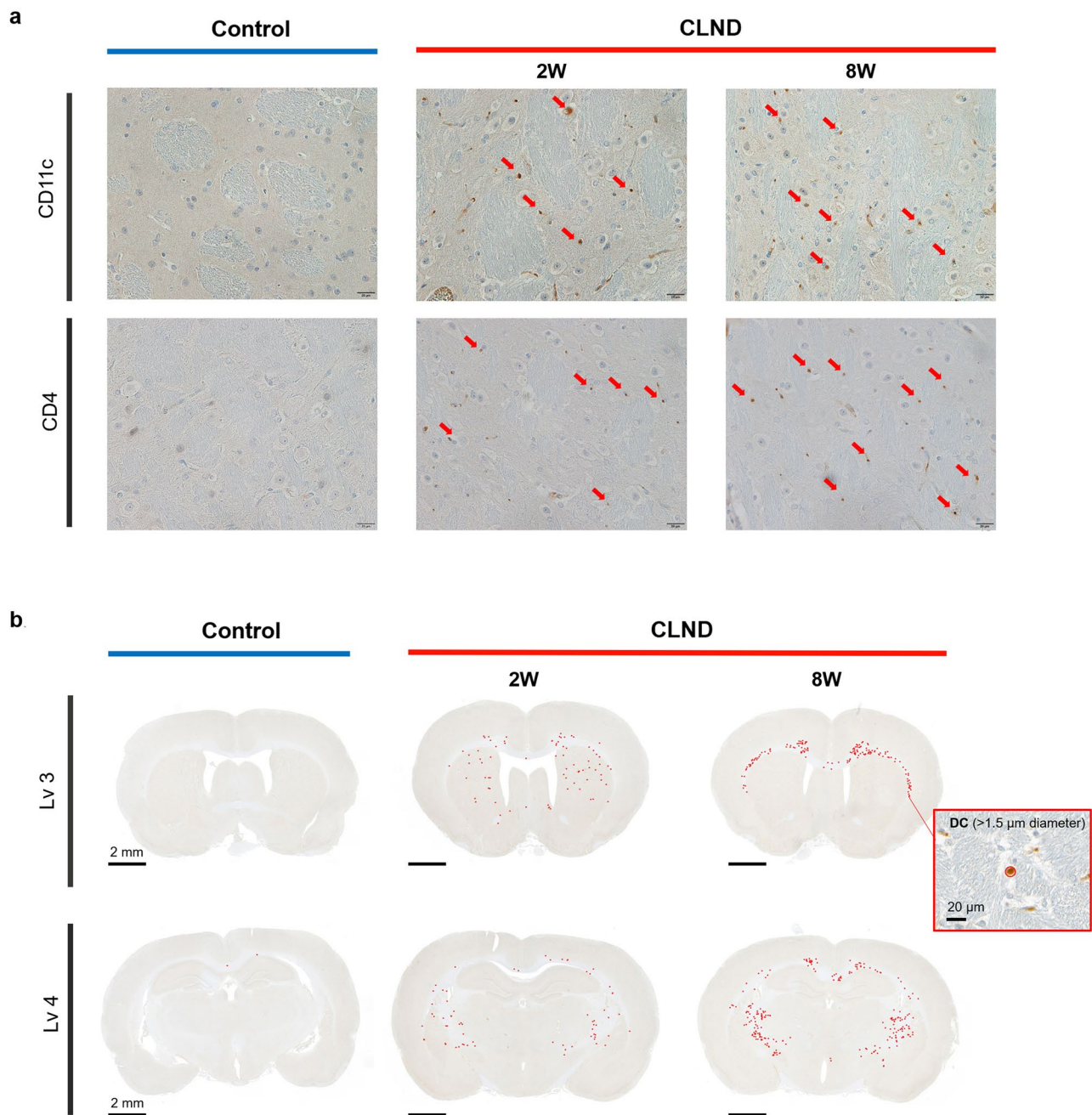


Fig. 6 Immunohistochemical tissue examination results for the investigation of immune cell distribution in the control and CLND groups. **(a)** CLND in animal brain sections marked with CD4 and CD11c in the ventricle-induced capsule (VIC) reveals immune cell infiltration (red arrows). The number of infiltrating immune cells increased over time from 2 weeks (2W) to 8 weeks (8W). **(b)** The image from each brain section represents dendritic cells (DCs) with a diameter larger than 1.5 μm, marked by red circles. DC count mainly increased in the white matter (WM)

441 s and 423 s at 2 and 8 weeks respectively, while the CLND group showed 225 s and 178 s at the same periods respectively. The average latency of fall decreased at 8 weeks compared to 2 weeks in the CLND group, but this difference was not statistically significant.

Discussion

We investigated the increased CSF levels within the ventricular system, increased brain tissue water content, corresponding histological alterations, and changes in animal behaviors due to peripheral lymphatic dysfunction in the head and neck (cervical) region. Although our animal model exhibited extreme lymphatic obstruction in the head and neck region compared to clinical

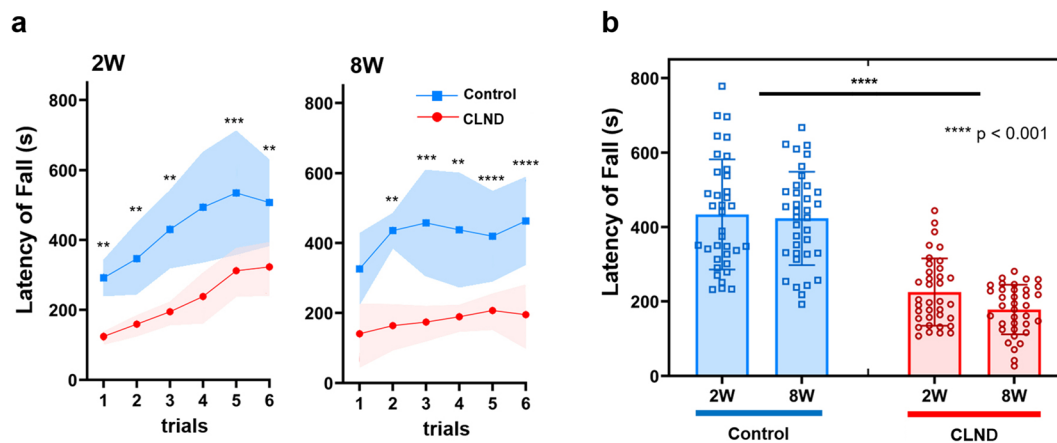


Fig. 7 Results of the rotarod test at 2 weeks and 8 weeks for the control and CLND groups. **(a)** Latency of fall times across 6 trials in each group ($n = 12$) during the rotarod test at 2 weeks (2 W) and 8 weeks (8 W) (t-test, ** $p < 0.01$, *** $p < 0.005$, and **** $p < 0.001$). **(b)** The average time in latency of fall at 2 W and 8 W for both groups. There was a significant difference between the control and the CLND group throughout the follow-up period (t-test, **** $p < 0.001$). However, no significant difference was observed between 2 W and 8 W within each group

conditions, it represents physiological conditions similar to those of patients with lymphatic injury from lymph node dissection and radiation therapy due to HNC.

Our imaging techniques enabled a more objective and quantitative assessment of these fluidic changes. MRI revealed that the LV volume size was further increased in CLND animals compared with control animals after 8 weeks, indicating CSF accumulation in the ventricular system. This resulted in cerebral histological changes similar to those observed in animal models of hydrocephalus. Histological examination revealed spaces between the tracts in the PVWM and a flattened lining of ependymal cells, akin to the results of a previous study [43]. Therefore, our animal model showed that hydrocephalus, ventricular enlargement, and compression of the surrounding tissues caused by abnormal CSF accumulation could be induced by lymphatic pathway disruption. THz spectroscopic imaging at the 0.5 THz revealed an overall increase in water content particularly around the ventricular region in the CLND group. The high sensitivity of the THz energy band in tissue water content was instrumental in visualizing the distribution of increased fluid accumulation in brain tissue resulting from lymphatic circulation disorders [42, 44–48]. The increase in LV volume and water content in the brain tissue also led to direct histological alterations. Decreased tissue density and widespread apoptotic features, such as shrunken nuclei and cellular edema, were observed in the CC of CLND animals. The results from our animal models demonstrated high water content and decreased tissue density which are highly consistent with cerebral edema [49]. According to previous literature, cerebral edema is a common consequence of ischemic brain injury [50, 51], and plays a critical role in determining prognosis in neurologic disorder [52–54]. Given that CSF

is a major component of brain tissue water content in cerebral edema [55, 56], the obstruction of CSF flow and the resulting volume increase could have contributed to the development of cerebral edema observed in our animal models.

Importantly, these changes were attributed to peripheral lymphatic obstruction regardless of the presence of ischemic injury or stroke. Indeed, extensive cell death, shrunken nuclei, and cellular edema were observed in a wide range of brain tissue sections, consistent with previous findings in animal models of cerebral venous sinus thrombosis [57]. Similar to insufficient venous drainage, insufficient lymphatic drainage can result in cerebral edema via blood-brain barrier disruption. These changes may have substantial implications in exacerbating neuropathological disorders with potentially harmful effects on cognition. Since the discovery of the lymphatic system of the CNS, the glymphatic and meningeal lymphatic systems have been shown to play crucial roles in the clearance of waste in the brain [58, 59]. It is increasingly clear that this role is associated with the occurrence of neurological diseases, as it is related to the clearance of lethal substances that trigger neurological disorders, such as beta-amyloid [10]. Consequently, there is a demonstrated correlation between neurological disorders and lymphatic circulation in the brain. The relationship between CLNs and CSF circulation has also been reported in various studies (Additional file 1: Figure S10a). Wang et al. used a DCLN model to demonstrate that the blockage of lymphatic circulation into CLNs interferes with cerebral beta-amyloid clearance, resulting in pathological features similar to Alzheimer's disease [60]. Kinota et al. observed a blockage of CSF drainage in a DCLN ligation model using dynamic MRI [61]. Moreover, a recent study reported that lymphatic vessels at the back of the

nose serve as a primary outflow pathway of CSF to CLNs, suggesting a close relationship between the function of CLNs and drainage of CSF [62] (Additional file 1: Figure S10b). Their results indicate that CLNs have a significant effect on CSF drainage. However, it remains unclear whether CSF drainage obstruction caused by peripheral lymphatic dysfunction directly leads to brain tissue alterations and how they impact behavior function. This study revealed that blockage of the lymphatic system in the head and neck region led to brain alterations. Consequently, this condition results in histopathological modifications resembling hydrocephalus and cerebral edema (Additional file 1: Figure S10c). We particularly consider that the alterations are associated with the inflammatory component of lymphedema.

Not only fluidic accumulation in the tissue but also the infiltration of immune cells is a key histopathological characteristic of lymphedema. The lymphedema condition occurs as an inflammatory response in lymph-accumulating regions, promoting immune cell migration [63–65]. Previous studies have demonstrated immune cell infiltration in animal models of lymphedema [19, 66, 67]. Our study revealed immune cell infiltration in the WM of CLND animals. This feature is similar to DCs accumulation in periventricular tissues due to autoimmune encephalitis, suggesting that lymphatic dysfunction in the head and neck region might induce the above-mentioned cerebral inflammatory responses. The infiltration of immune cells was similar to that observed in animals with extremity lymphedema [68]. Our finding demonstrated histopathological changes in the animal models associated with mild cerebral edema and hydrocephalus, but the increase in water content and immune cell infiltration in the brain tissue resembled the typical characteristics of lymphedema itself. These changes were shown to affect the motor activity of the animals in our experiment. According to changes in water content and tissue alteration in the brain appeared at 2 weeks, the reduced performance of the animals at the same time suggests that these changes in the brain directly influenced their behavior. The previous studies with animal models that exhibited the pathophysiological changes of cerebral edema and hydrocephalus also showed a significant reduction in the latency of falls in rotarod tests similar to our results [69, 70]. While those studies involved models with direct intervention to the ventricles that blocked CSF circulation, our model uniquely obstructed lymphatic circulation to the periphery lymph nodes. This indicates that peripheral lymphatic circulation in the head and neck region significantly impacts CSF drainage in the brain, and its dysfunction may have more severe consequences compared to extremities lymphedema.

In clinical practice, lymphatic malfunction has been observed in patients who underwent HNC treatment.

Head and neck lymphedema often occurs as a secondary condition characterized by the abnormal accumulation of lymphatic fluid in the tissues of the head and neck following treatment. Additionally, abnormalities in cognitive function have been reported in these patients [71–73]. Historically, edema of the neck, face, tongue, and oral cavity was considered a primary sign of head and neck lymphedema in patients with HNC who had undergone chemotherapy, radiotherapy, and CLND [74–76]. Our findings suggest that surgical procedures with CLND may also be a risk factor for brain damage and activity decline due to lymphatic dysfunction, similar to the brain fog or brain damage observed in those undergoing chemotherapy or radiation therapy [77, 78]. We observed that swelling and abnormal lymphatic drainage were maintained for up to 8 weeks, and it indicates that lymphatic obstruction was not resolved during the follow-up period. However, our animal model was close to an acute lymphatic obstruction model. This contrasts with the chronic characteristics of head and neck lymphedema typically seen in clinical settings. Therefore, while our model provides insights into early-stage lymphatic dysfunction, it did not fully replicate the long-term, chronic lymphatic dysfunction observed in patients.

In this respect, there are limitations to this study. This study was unable to determine whether the impact of lymphatic dysfunction on the brain is transient or permanent. This is a critical aspect to explore in future research, as it could provide key information on when interventions of rehabilitation should be introduced for patients undergoing HNC treatment who are at risk of complications. Understanding the temporal characteristics of these effects will be essential for optimizing patient care and improving outcomes. Next, the bilateral CLND is not commonly performed in the clinical setting. Although bilateral treatment is not the most common clinical condition, we adopted this model to ensure that the effects of lymphatic dysfunction in the head and neck region on brain pathology and behavior could be clearly demonstrated. Future studies should explore the impact of unilateral lymphatic dysfunction and its clinical relevance to refine our understanding of the relationship between lymphatic circulation and neurophysiological changes. Consequently, the impact on the brain may not be significant in patients with early-stage lymphatic obstruction. Lymphatic circulation disorders can lead to disease-inducing changes a lifelong condition. Future research should include detailed research to obtain precise results and clinical studies that track the cognitive and physical functions of patients with lymphatic dysfunction in the head and neck region. However, our findings suggest that patients who develop head and neck lymphedema or exhibit signs of severe impaired lymphatic drainage should be considered for appropriate interventions, such

as alternative shunting or bypass, to mitigate potential complications.

Conclusions

Our study demonstrated through animal experiments that peripheral lymphatic dysfunction in the head and neck region can cause critical alterations in the brain, potentially leading to behavioral impairments. These findings highlight a previously underappreciated potential risk factor of brain damage in HNC patients, procedures of CLND. Furthermore, it provided the link between the peripheral lymphatic system and neurological disorder progress for future research in cancer patient management. Although our study represents an important step, further investigations are necessary to fully elucidate the complex relationships between lymphatic circulation and neurological disorders.

Abbreviations

HNC	head and neck cancer
CLND	cervical lymph node dissection
CNS	central nervous system
SCLN	superficial cervical lymph node
DCLN	deep cervical lymph node
CSF	cerebrospinal fluid
THz	terahertz
NIRF-ICGL	near-infrared fluorescence indocyanine green lymphangiography
ICG	indocyanine green
FFT	fast Fourier transform
LV	lateral ventricles
TV	third ventricle
H&E	hematoxylin and eosin
IHC	immunohistochemistry
DC	dendritic cell
M	meninges
CC	cerebral cortex
WM	white matter
PVWM	periventricular white matter
VIC	ventral internal capsule

Supplementary Information

The online version contains supplementary material available at <https://doi.org/10.1186/s40478-025-01953-w>.

Supplementary Material 1

Acknowledgements

This work was supported by the National Research Foundation of Korea (NRF) grant funded by the Korean government (MSIT) (No. RS-2024-00338179 and RS-2024-00454894), and a grant (2022IF0021) from the Asan Institute for Life Sciences and Corporate Relations of Asan Medical Center, Seoul, Korea. Prof. Won Kim and researcher Dabin Ko provided valuable assistance in operating the rotarod equipment, which was instrumental in obtaining the study's results. We thank the core facilities of the Comparative Pathology Laboratory and Animal Experiment Laboratory at the Convergence mEDicine research center (CREDIT), Asan Medical Center, for sharing their equipment, services, and expertise with us.

Author contributions

H. Cheon designed the research and sample models, performed the experiments, analyzed the data, and prepared the draft manuscript. D. C. Woo performed an MR imaging experiment, analyzed the MR imaging data,

and discussed them. Y. J. Chae supported analyzing the MR data. I. Maeng performed THz spectroscopic imaging and supported analyzing THz data. S. Cha analyzed the histological data and added its clinical significance. S. J. Oh and J. Y. Jeon analyzed the data, coordinated the research, acquired research funding, and supervised the project. All authors have reviewed the results and approved the final version of the manuscript. The illustrations used in the figures were created by H. Cheon with the help of the Medical Contents Center of Asan Medical Center.

Funding

National Research Foundation of Korea (NRF): No. RS-2024-00338179, No. RS-2024-00454894. Asan Institute for Life Sciences and Corporate Relations of Asan Medical Center: 2022IF0021.

Data availability

No datasets were generated or analysed during the current study.

Declarations

Ethics approval and consent to participate

This study was performed based on preclinical animal experiments and does not involve human-derived materials or clinical studies in the research process. The number of animals and all animal procedures in this study were approved and regulated by the Institutional Animal Care and Use Committee (IACUC) of the Asan Institute for Life Sciences, Asan Medical Center (# 2022-12-110 and 2023-30-226). The IACUC abides by the relevant guidelines including the ILAR and ARRIVE guidelines.

Consent for publication

Not applicable.

Competing interests

The authors declare no competing interests.

Received: 26 December 2024 / Accepted: 9 February 2025

Published online: 08 April 2025

References

1. Sung H, Ferlay J, Siegel RL, Laversanne M, Soerjomataram I, Jemal A, Bray F (2021) Global Cancer statistics 2020: GLOBOCAN estimates of incidence and mortality worldwide for 36 cancers in 185 countries. *CA Cancer J Clin* 71(3):209–249. <https://doi.org/10.3322/caac.21660>
2. Demos-davies K, Lawrence J, Rogich A, Lind E, Seelig D, Strohl JJ, Demos-davies K (2023) Cancer treatment induces neuroinflammation and behavioral deficits in mice. *Front Behav Neurosci* 16:1067298. <https://doi.org/10.3389/fnbeh.2022.1067298>
3. Was H, Borkowska A, Bagues A, Tu L, Liu JYH, Lu Z, Rudd JA, Nurgali K, Abalo R (2022) Mechanisms of Chemotherapy-Induced neurotoxicity. *Front Pharmacol* 13:750507. <https://doi.org/10.3389/fphar.2022.750507>
4. Ma Q, Ineichen BV, Detmar M, Proulx ST (2017) Outflow of cerebrospinal fluid is predominantly through lymphatic vessels and is reduced in aged mice. *Nat Commun* 8(1):1434. <https://doi.org/10.1038/s41467-017-01484-6>
5. Suami H (2016) Lymphosome concept: anatomical study of the lymphatic system. *J Surg Oncol* 115(1):13–17. <https://doi.org/10.1002/jso.24332>
6. das Neves SP, Delivanoglou N, Da Mesquita S (2021) CNS-draining meningeal lymphatic vasculature: roles, conundrums and future challenges. *Front Pharmacol* 12:655052. <https://doi.org/10.3389/fphar.2021.655052>
7. Jiang H, Wei H, Zhou Y, Xiao X, Zhou C, Ji X (2022) Overview of the meningeal lymphatic vessels in aging and central nervous system disorders. *Cell Biosci* 12(1):202. <https://doi.org/10.1186/s13578-022-00942-z>
8. Louveau A, Plog BA, Antila S, Alitalo K, Nedergaard M, Kipnis J (2017) Understanding the functions and relationships of the glymphatic system and meningeal lymphatics. *J Clin Invest* 127(9):3210–3219. <https://doi.org/10.1172/JCI90603>
9. Louveau A, Herz J, Alme MN, Salvador AF, Dong MQ, Viar KE, Herod SG, Knopp J, Setliff JC, Lupi AL, Da Mesquita S, Frost EL, Gaultier A, Harris TH, Cao R, Hu S, Lukens JR, Smirnov I, Overall CC, Oliver G, Kipnis J (2018) CNS lymphatic drainage and neuroinflammation are regulated by meningeal lymphatic

- vasculature. *Nat Neurosci* 21(10):1380–1391. <https://doi.org/10.1038/s4159-3-018-0227-9>
10. Ahn JH, Cho H, Kim J-H, Kim SH, Ham J-S, Park I, Suh SH, Hong SP, Song J-H, Hong Y-K, Jeong Y, Park S-H, Koh GY (2019) Meningeal lymphatic vessels at the skull base drain cerebrospinal fluid. *Nature* 572(7767):62–66. <https://doi.org/10.1038/s41586-019-1419-5>
 11. Chachaj A, Gašiorowski K, Szuba A, Sieradzki A, Leszek J (2023) The lymphatic system in the brain clearance mechanisms - new therapeutic perspectives for Alzheimer's disease. *Curr Neuropharmacol* 21(1):380–391. <https://doi.org/10.2174/1570159X20666220411091332>
 12. Tarasoff-Conway JM, Carare RO, Osorio RS, Glodzik L, Butler T, Fieremans E, Axel L, Rusinek H, Nicholson C, Zlokovic BV, Frangione B, Blennow K, Ménard J, Zetterberg H, Wisniewski T, De Leon MJ (2015) Clearance systems in the brain - implications for Alzheimer disease. *Nat Rev Neurol* 11(8):457–470. <https://doi.org/10.1038/nrneuro.2015.119>
 13. Wang D, Chen F, Han Z, Yin Z, Ge X, Lei P (2021) Relationship between amyloid- β deposition and blood-brain barrier dysfunction in Alzheimer's disease. *Front Cell Neurosci* 15:695479. <https://doi.org/10.3389/fncel.2021.695479>
 14. Da Mesquita S, Louveau A, Vaccari A, Smirnov I, Cornelison RC, Kingsmore KM, Contarino C, Onengut-Gumusc S, Farber E, Raper D, Viar KE, Powell RD, Baker W, Dabhi N, Bai R, Cao R, Hu S, Rich SS, Munson JM, Lopes MB, Overall CC, Acton ST, Kipnis J (2018) Functional aspects of meningeal lymphatics in ageing and Alzheimer's disease. *Nature* 560(7717):185–191. <https://doi.org/10.1038/s41586-018-0368-8>
 15. Li D, Lin H, Sun S, Liu S, Liu Z, He Y, Zhu J, Xu J, Semyachkina-Glushkovskaya O, Yu T, Zhu D (2023) Photostimulation of lymphatic clearance of β -amyloid from mouse brain: a new strategy for the therapy of Alzheimer's disease. *Front Optoelectron* 16(1):45. <https://doi.org/10.1007/s12200-023-00099-8>
 16. Mentis A-FA, Dardiotis E, Chrousos GP (2021) Apolipoprotein E4 and meningeal lymphatics in Alzheimer disease: a conceptual framework. *Mol Psychiatry* 26(4):1075–1097. <https://doi.org/10.1038/s41380-020-0731-7>
 17. Rego S, Sanchez G, Da Mesquita S (2023) Current views on meningeal lymphatics and immunity in aging and Alzheimer's disease. *Mol Neurodegener* 18(1):55. <https://doi.org/10.1186/s13024-023-00645-0>
 18. Kataru RP, Baik JE, Park HJ, Wiser I, Rehal S, Shin JY, Mehrara BJ (2019) Regulation of immune function by the lymphatic system in lymphedema. *Front Immunol* 10:470. <https://doi.org/10.3389/fimmu.2019.00470>
 19. Nishioka T, Katayama K, Kumegawa S, Isono K, Baba T, Tsujimoto H, Yamada G, Inoue N, Asamura S (2023) Increased infiltration of CD4+T cell in the complement deficient lymphedema model. *BMC Immunol* 24:42. <https://doi.org/10.1186/s12865-023-00580-1>
 20. Bucan A, Frensdø M, Ngo MT, Sørensen JA, Hölmich LR (2023) Surgical lymphedema models in the mice hindlimb—A systematic review and quality assessment. *Microsurgery* 44(1):e31088. <https://doi.org/10.1002/micr.31088>
 21. Cheon H, Gelvosa MN, Kim SA, Song HY, Jeon JY (2023) Lymphatic channel sheet of polydimethylsiloxane for preventing secondary lymphedema in the rat upper limb model. *Bioeng Transl Med* 8(1):e10371. <https://doi.org/10.1002/btm2.10371>
 22. Kim SA, Gelvosa MN, Cheon H, Jeon JY (2023) The effects of postoperative treadmill exercise on rats with secondary lymphedema. *PLoS ONE* 18(5):e0285384. <https://doi.org/10.1371/journal.pone.0285384>
 23. Yang C-Y, Nguyen DH, Wu CW, Fang YHD, Chao KT, Patel KM, Cheng MH (2014) Developing a lower limb lymphedema animal model with combined lymphadenectomy and low-dose radiation. *Plast Reconstr Surg* 2(3):1–6. <https://doi.org/10.1097/GOX.0000000000000064>
 24. Daneshgaran G, Lo AY, Paik CB, Cooper MN, Sung C, Jiao W, Park SY, Ni P, Yu RP, Vorobyova I, Jashashvili T, Hong Y-K, Kim GH, Conti PS, Chai Y, Wong AK (2019) A pre-clinical animal model of secondary head and neck lymphedema. *Sci Rep* 9(1):18264. <https://doi.org/10.1038/s41598-019-54201-2>
 25. Visconti G, Brunelli C, Mulè A, Franceschini G, Chen H-C, Masetti R, Salgarello M (2016) Septum-based cervical lymph-node free flap in rat: a new model. *J Surg Res* 201(1):1–12. <https://doi.org/10.1016/j.jss.2015.09.027>
 26. Aksoyler D, Bitik O, Menku Ozdemir FD, Gokoz O, Uzun H, Yenicieri B, Nasir SN (2021) A new experimental lymphedema model: reevaluating the efficacy of rat models and their clinical translation for chronic lymphedema studies. *Ann Plast Surg* 86(6):707–713. <https://doi.org/10.1097/SAP.0000000000002479>
 27. Hadrian R, Palmes D (2017) Animal models of secondary lymphedema: new approaches in the search for therapeutic options. *Lymphat Res Biol* 15(1):2–16. <https://doi.org/10.1089/lrb.2016.0015>
 28. Cheon H, Lee S-H, Kim SA, Kim B, Suh HP, Jeon JY (2023) In vivo dynamic and static analysis of lymphatic dysfunction in lymphedema using near-infrared fluorescence indocyanine green lymphangiography. *Arterioscler Thromb Vasc Biol* 43(10):2008–2022. <https://doi.org/10.1161/ATVBAHA.123.319188>
 29. Maus EA, Tan I, Rasmussen JC, Marshall MV, Fife CE, Smith LA, Guilliod R, Sevick-Muraca EM (2012) Near-infrared fluorescence imaging of lymphatics in head and neck lymphedema. *Head Neck* 34(3):448–453. <https://doi.org/10.1002/hed.21538>
 30. Narushima M, Yamamoto T, Ogata F, Yoshimatsu H, Mihara M, Koshima I (2015) Indocyanine green lymphography findings in limb lymphedema. *J Reconstr Microsurg* 32(1):72–79. <https://doi.org/10.1055/s-0035-1564608>
 31. Cheon H, Kim SA, Kim B, Jeon JY (2023) Investigation of optimizing indocyanine green solution for in vivo lymphatic research using near-infrared fluorescence indocyanine green lymphangiography. *Sci Rep* 13(1):14966. <https://doi.org/10.1038/s41598-023-40826-x>
 32. Krishnamurthy S, Li J, Schultz L, McAllister JP (2009) Intraventricular infusion of hyperosmolar dextran induces hydrocephalus: a novel animal model of hydrocephalus. *Cerebrospinal Fluid Res* 6:16. <https://doi.org/10.1186/1743-8454-6-16>
 33. McAllister JP, Talcott MR, Isaacs AM, Zwick SH, Garcia-Bonilla M, Castaneyra-Ruiz L, Hartman AL, Dilger RN, Fleming SA, Golden RK, Morales DM, Harris CA, Limbrick DD (2021) A novel model of acquired hydrocephalus for evaluation of neurosurgical treatments. *Fluids Barriers CNS* 18(1):49. <https://doi.org/10.1186/s12987-021-00281-0>
 34. Lee K, Jeoung K, Kim SH, Ji Y, Son H, Choi Y, Huh Y-M, Suh J-S, Oh SJ (2018) Measuring water contents in animal organ tissues using terahertz spectroscopic imaging. *Biomed Opt Express* 9(4):1582. <https://doi.org/10.1364/BOE.9.001582>
 35. Hernandez-Cardoso GG, Amador-Medina LF, Gutierrez-Torres G, Reyes-Reyes ES, Benavides Martínez CA, Cardona Espinoza C, Arce Cruz J, Salas-Gutierrez I, Murillo-Ortiz BO, Castro-Camus E (2022) Terahertz imaging demonstrates its diagnostic potential and reveals a relationship between cutaneous dehydration and neuropathy for diabetic foot syndrome patients. *Sci Rep* 12(1):3110. <https://doi.org/10.1038/s41598-022-06996-w>
 36. Ji YB, Moon I-S, Bark HS, Kim SH, Park DW, Noh SK, Huh Y-M, Suh J-S, Oh SJ, Jeon T-I (2016) Terahertz otoscope and potential for diagnosing otitis media. *Biomed Opt Express* 7(4):1201–1209. <https://doi.org/10.1364/BOE.7.001201>
 37. Shi S, Yuan S, Zhou J, Jiang P (2023) Terahertz technology and its applications in head and neck diseases. *iScience* 26(7):107060. <https://doi.org/10.1016/j.isci.2023.107060>
 38. Garman RH, Li AA, Kaufmann W, Auer RN, Bolon B (2016) Recommended methods for brain processing and quantitative analysis in rodent developmental neurotoxicity studies. *Toxicol Pathol* 44(1):14–42. <https://doi.org/10.1177/0192623315596858>
 39. Rao DB, Little PB, Malarkey DE, Herbert RA, Sills RC (2011) Histopathological evaluation of the nervous system in national toxicology program rodent studies. *Toxicol Pathol* 39(3):463–470. <https://doi.org/10.1177/0192623311401044>
 40. Fitzgerald AJ, Pickwell-MacPherson E, Wallace VP (2014) Use of finite difference time domain simulations and Debye theory for modelling the terahertz reflection response of normal and tumour breast tissue. *PLoS ONE* 9(7):e99291. <https://doi.org/10.1371/journal.pone.0099291>
 41. Ge H, Sun Z, Jiang Y, Wu X, Jia Z, Cui G, Zhang Y (2023) Recent advances in THz detection of water. *Int J Mol Sci* 24(13):10936. <https://doi.org/10.3390/ijm241310936>
 42. Yan Z, Zhu L-G, Meng K, Huang W, Shi Q (2022) THz medical imaging: from in vitro to in vivo. *Trends Biotechnol* 40(7):816–830. <https://doi.org/10.1016/j.tibtech.2021.12.002>
 43. Jugé L, Pong AC, Bongers A, Sinkus R, Bilston LE, Cheng S (2016) Changes in rat brain tissue microstructure and stiffness during the development of experimental obstructive hydrocephalus. *PLoS ONE* 11(2):1–24. <https://doi.org/10.1371/journal.pone.0148652>
 44. Cheon H, Yang H, Son J (2017) Toward clinical cancer imaging using terahertz spectroscopy. *IEEE J Sel Top Quantum Electron* 23(4):1–9. <https://doi.org/10.1109/JSTQE.2017.2704905>
 45. Jepsen PU, Cooke DG, Koch M (2011) Terahertz spectroscopy and imaging—modern techniques and applications. *Laser Photon Rev* 5(1):124–166. <https://doi.org/10.1002/lpor.201000011>
 46. Parrott EPJ, Sun Y, Pickwell-MacPherson E (2011) Terahertz spectroscopy: its future role in medical diagnoses. *J Mol Struct* 1006:66–76. <https://doi.org/10.1016/j.molstruc.2011.05.048>
 47. Sadeghi A, Naghavi SMH, Mozafari M, Afshari E (2023) Nanoscale biomaterials for terahertz imaging: a non-invasive approach for early cancer detection. *Transl Oncol* 27:101565. <https://doi.org/10.1016/j.tranon.2022.101565>

48. Yu L, Hao L, Meiqiong T, Jiaoqi H, Wei L, Jinying D, Xueping C, Weiling F, Yang Z (2019) The medical application of terahertz technology in non-invasive detection of cells and tissues: opportunities and challenges. *RSC Adv* 9(17):9354–9363. <https://doi.org/10.1039/C8RA10605C>
49. Chen S, Shao L, Ma L (2021) Cerebral edema formation after stroke: emphasis on blood–brain barrier and the lymphatic drainage system of the brain. *Front Cell Neurosci* 15:716825. <https://doi.org/10.3389/fncel.2021.716825>
50. Dalby T, Wohl E, Dinsmore M, Unger Z, Chowdhury T, Venkatraghavan L (2021) Pathophysiology of cerebral edema—A comprehensive review. *J Neuroanaesth Crit Care* 8:163–172. <https://doi.org/10.1055/s-0040-1721165>
51. Han W, Song Y, Rocha M, Shi Y (2023) Ischemic brain edema: emerging cellular mechanisms and therapeutic approaches. *Neurobiol Dis* 178:106029. <https://doi.org/10.1016/j.nbd.2023.106029>
52. Eyleten C, Sharif L, Wicik Z, Jakubik D, Jarosz-Popek J, Soplinska A, Postula M, Czlonkowska A, Kaplon-Cieslicka A, Mirowska-Guzel D (2021) The relation of the brain-derived neurotrophic factor with microRNAs in neurodegenerative diseases and ischemic stroke. *Mol Neurobiol* 58(1):329–347. <https://doi.org/10.1007/s12035-020-02101-2>
53. Glaser NS, Wootton-Gorges SL, Kim I, Tancredi DJ, Marcin JP, Muir A, Kuppermann N (2017) Regional brain water content and distribution during diabetic ketoacidosis. *J Pediatr* 180:170–176. <https://doi.org/10.1016/j.jpeds.2016.09.003>
54. Jha RM, Raikwar SP, Mihaljevic S, Casabella AM, Catapano JS, Rani A, Desai S, Gerzanich V, Simard JM (2021) Emerging therapeutic targets for cerebral edema. *Expert Opin Ther Targets* 25(11):917–938. <https://doi.org/10.1080/14728222.2021.2010045>
55. Dhar R, Chen Y, Hamzehloo A, Kumar A, Heitsch L, He J, Chen L, Slowik A, Strbian D, Lee J-M (2020) Reduction in cerebrospinal fluid volume as an early quantitative biomarker of cerebral edema after ischemic stroke. *Stroke* 51(2):462–467. <https://doi.org/10.1161/STROKEAHA.119.027895>
56. Du T, Mestre H, Kress BT, Liu G, Sweeney AM, Samson AJ, Rasmussen MK, Mortensen KN, Bork PAR, Peng W, Olveda GE, Bashford L, Toro ER, Tithof J, Kelley DH, Thomas JH, Hjorth PG, Martens EA, Mehta RI, Hirase H, Mori Y, Nedergaard M (2022) Cerebrospinal fluid is a significant fluid source for anoxic cerebral oedema. *Brain* 145(2):787–797. <https://doi.org/10.1093/brain/awab293>
57. Bourrienne M-C, Loyau S, Benichi S, Gay J, Solo-Nomenjanahary M, Journé C, Di Meglio L, von Freiherr A, Desilles J-P, Ho-Tin-Noé B, Aizenberg N, Mazighi M (2021) A novel mouse model for cerebral venous sinus thrombosis. *Transl Stroke Res* 12(6):1055–1066. <https://doi.org/10.1007/s12975-021-00898-1>
58. Aspelund A, Antila S, Proulx ST, Karlsen TV, Karaman S, Detmar M, Wiig H, Alitalo K (2015) A dural lymphatic vascular system that drains brain interstitial fluid and macromolecules. *J Exp Med* 212(7):991–999. <https://doi.org/10.1084/jem.20142290>
59. Louveau A, Smirnov I, Keyes TJ, Eccles JD, Rouhani SJ, Peske JD, Derecki NC, Castle D, Mandell JW, Lee KS, Harris TH, Kipnis J (2015) Structural and functional features of central nervous system lymphatic vessels. *Nature* 523(7560):337–341. <https://doi.org/10.1038/nature14432>
60. Wang L, Zhang Y, Zhao Y, Marshall C, Wu T, Xiao M (2019) Deep cervical lymph node ligation aggravates AD-like pathology of APP/PS1 mice. *Brain Pathol* 29(2):176–192. <https://doi.org/10.1111/bpa.12656>
61. Kinota N, Kameda H, Xiawei B, Fujii T, Kato D, Takahashi B, Morita R, Abo D, Majima R, Ishii H, Minowa K, Kudo K (2023) Blockage of CSF outflow in rats after deep cervical lymph node ligation observed using Gd-based MR imaging. *Magn Reson Med Sci* 23(4):449–459. <https://doi.org/10.2463/mrms.mp.2023-0023>
62. Yoon J-H, Jin H, Kim HJ, Hong SP, Yang MJ, Ahn JH, Kim Y-C, Seo J, Lee Y, McDonald DM, Davis MJ, Koh GY (2024) Nasopharyngeal lymphatic plexus is a hub for cerebrospinal fluid drainage. *Nature* 625(7996):768–777. <https://doi.org/10.1038/s41586-023-06899-4>
63. Ghanta S, Cuzzone DA, Torrisi JS, Albano NJ, Joseph WJ, Savetsky IL, Gardenier JC, Chang D, Zampell JC, Mehrara BJ (2015) Regulation of inflammation and fibrosis by macrophages in lymphedema. *Am J Physiol Heart Circ Physiol* 308(9):H1065–H1077. <https://doi.org/10.1152/ajpheart.00598.2014>
64. Kataru RP, Wiser I, Baik JE, Park HJ, Rehal S, Shin JY, Mehrara BJ (2019) Fibrosis and secondary lymphedema: chicken or egg? *Transl Res* 209:68–76. <https://doi.org/10.1016/j.trsl.2019.04.001>
65. Li CY, Kataru RP, Mehrara BJ (2020) Histopathologic features of lymphedema: a molecular review. *Int J Mol Sci* 21(7):2546. <https://doi.org/10.3390/ijms21072546>
66. García Nores GD, Ly CL, Cuzzone DA, Kataru RP, Hesse GE, Torrisi JS, Huang JJ, Gardenier JC, Savetsky IL, Nitti MD, Yu JZ, Rehal S, Mehrara BJ (2018) CD4+ T cells are activated in regional lymph nodes and migrate to skin to initiate lymphedema. *Nat Commun* 9(1):1970. <https://doi.org/10.1038/s41467-018-04418-y>
67. Gousopoulos E, Proulx ST, Scholl J, Uecker M, Detmar M (2016) Prominent lymphatic vessel hyperplasia with orofegressive dysfunction and distinct immune cell infiltration in lymphedema. *Am J Pathol* 186(8):2193–2203. <https://doi.org/10.1016/j.ajpath.2016.04.006>
68. Clarkson BD, Walker A, Harris M, Rayasam A, Sandor M, Fabry Z (2014) Mapping the accumulation of co-infiltrating CNS dendritic cells and encephalitogenic T cells during EAE. *J Neuroimmunol* 277(1–2):39–49. <https://doi.org/10.1016/j.jneuroim.2014.09.016>
69. Chen K-W, Chen Y-R, Yang L-Y, Cheng Y-W, Chou S-C, Chen Y-H, Chen Y-T, Hsieh S-T, Kuo M-F, Wang K-C (2024) Microcirculatory impairment and cerebral injury in hydrocephalus and the effects of cerebrospinal fluid diversion. *Neurosurgery* 95(2):469–479. <https://doi.org/10.1227/neu.0000000000002908>
70. McMullen AB, Baidwan GS, McCarthy KD (2012) Morphological and behavioral changes in the pathogenesis of a novel mouse model of communicating hydrocephalus. *PLoS ONE* 7(1):e30159. <https://doi.org/10.1371/journal.pone.0030159>
71. AM W, JE B, JY HPCL, RP S, BJ K M (2021) Docetaxel causes lymphatic endothelial cell apoptosis and impairs lymphatic function and gene expression in vitro. *J Transl Sci* 7:1–6. <https://doi.org/10.15761/JTS.1000402>
72. Hermelink K (2015) Chemotherapy and cognitive function in breast cancer patients: the so-called chemo brain. *J Natl Cancer Inst Monogr* 2015(51):67–69. <https://doi.org/10.1093/jncimonographs/igv009>
73. Warrington JP, Csiszar A, Mitschelen M, Lee YW, Sonntag WE (2012) Whole brain radiation-induced impairments in learning and memory are time-sensitive and reversible by systemic hypoxia. *PLoS ONE* 7(1):e30444. <https://doi.org/10.1371/journal.pone.0030444>
74. Mcgarvey AC, Osmotherly PG, Hoffman GR, Chiarelli PE (2014) Lymphoedema following treatment for head and neck cancer: impact on patients, and beliefs of health professionals. *Eur J Cancer Care (Engl)* 23:317–327. <https://doi.org/10.1111/ecc.12134>
75. Smith BG, Lewin JS (2010) Lymphedema management in head and neck cancer. *Curr Opin Otolaryngol Head Neck Surg* 18(3):153–158. <https://doi.org/10.1097/MOO.0b013e3283393799>
76. Smith BG, Hutcheson KA, Little LG, Skoracki RJ, Rosenthal DI, Lai SY, Lewin JS (2015) Lymphedema outcomes in patients with head and neck cancer. *Otolaryngol Neck Surg* 152(2):284–291. <https://doi.org/10.1177/0194599814558402>
77. Abdelsalam RM, Hamam HW, Eissa NM, El-Sahar AE, Essam RM (2024) Empagliflozin dampens doxorubicin-induced chemobrain in rats: the possible involvement of oxidative stress and PI3K/Akt/mTOR/NF-κB/TNF-α signaling pathways. *Mol Neurobiol*. <https://doi.org/10.1007/s12035-024-04499-5>
78. Philippot G, Stenerlöv B, Fredriksson A, Sundell-Bergman S, Eriksson P, Buratovic S (2019) Developmental effects of neonatal fractionated co-exposure to low-dose gamma radiation and paraquat on behaviour in adult mice. *J Appl Toxicol* 39(4):582–589. <https://doi.org/10.1002/jat.3748>

Publisher's note

Springer Nature remains neutral with regard to jurisdictional claims in published maps and institutional affiliations.